ARTICLE IN PRESS
Computer Physics Communications ▮ (▮▮▮▮) ▮▮▮–▮▮▮

Contents lists available at ScienceDirect

Computer Physics Communications

journal homepage: www.elsevier.com/locate/cpc

A generalized crystal-cutting method for modeling arbitrarily oriented crystals in 3D periodic simulation cells with applications to crystal–crystal interfaces

Matthew P. Kroonblawd, Nithin Mathew, Shan Jiang, Thomas D. Sewell [*]

Department of Chemistry, University of Missouri-Columbia, Columbia, MO 65211-7600, USA

ARTICLE INFO

Article history:
Received 31 March 2016
Received in revised form
18 May 2016
Accepted 2 July 2016
Available online xxxx

Keywords:
Anisotropy
Surfaces
Crystal defects
Atomistic simulations
Periodic boundary conditions

ABSTRACT

A Generalized Crystal-Cutting Method (GCCM) is developed that automates construction of three-dimensionally periodic simulation cells containing arbitrarily oriented single crystals and thin films, two-dimensionally (2D) infinite crystal–crystal homophase and heterophase interfaces, and nanostructures with intrinsic N-fold interfaces. The GCCM is based on a simple mathematical formalism that facilitates easy definition of constraints on cut crystal geometries. The method preserves the translational symmetry of all Bravais lattices and thus can be applied to any crystal described by such a lattice including complicated, low-symmetry molecular crystals. Implementations are presented with carefully articulated combinations of loop searches and constraints that drastically reduce computational complexity compared to simple loop searches. Orthorhombic representations of monoclinic and triclinic crystals found using the GCCM overcome some limitations in standard distributions of popular molecular dynamics software packages. Stability of grain boundaries in β-HMX was investigated using molecular dynamics and molecular statics simulations with 2D infinite crystal–crystal homophase interfaces created using the GCCM. The order of stabilities for the four grain boundaries studied is predicted to correlate with the relative prominence of particular crystal faces in lab-grown β-HMX crystals. We demonstrate how nanostructures can be constructed through simple constraints applied in the GCCM framework. Example GCCM constructions are shown that are relevant to some current problems in materials science, including shock sensitivity of explosives, layered electronic devices, and pharmaceuticals.

1. Introduction

Molecular dynamics (MD) and related particle-based simulation methods are indispensable tools in the study of crystal anisotropy [1–10], surfaces [10–13], defects [14–19], and crystal–crystal interfaces such as grain boundaries [20–27] and heterophase interfaces [28–30]. Many of these studies [14–24,27,29,30] have focused on materials with comparatively 'simple' and highly symmetric (*e.g.*, cubic) packing structures, including atomic crystals of metals, ceramics, and traditional semiconductors such as gallium arsenide. However, a wide range of technologically relevant molecular materials, including pharmaceuticals [31,32], high explosives [33–36], and organic semiconductors [37,38], exhibit packing structures with significantly lower symmetry and often crystallize in monoclinic and triclinic forms. Low-symmetry crystal systems, especially the monoclinic and triclinic systems, can complicate the construction of simulation cells that involve oriented thin films, grain boundaries, and crystal–crystal interfaces. Examples from materials science range from engineering layered electronic devices [3,22,26,29,30] to predicting the shock response and detonation sensitivity of explosives [5,6,8,28]. We present here a Generalized Crystal-Cutting Method (GCCM) that enables and practically automates facile construction of simulation cells containing oriented crystalline thin films and crystal–crystal interfaces.

Many MD simulations of crystals employ three-dimensional (3D) periodic boundary conditions (PBCs), which lead to simulation geometries corresponding to infinite stacks of thin films or 'bulk' material. An implicit requirement for the use of PBCs in crystal simulations is that the simulation cell exactly preserves the crystal translational symmetry. For this reason, low-symmetry crystals with monoclinic and triclinic Bravais lattices are often modeled in non-orthorhombic parallelepiped-shaped simulation cells. This

---

[*] Corresponding author.
E-mail address: SewellT@missouri.edu (T.D. Sewell).

http://dx.doi.org/10.1016/j.cpc.2016.07.007
0010-4655/© 2016 Elsevier B.V. All rights reserved.

Please cite this article in press as: M.P. Kroonblawd, et al., A generalized crystal-cutting method for modeling arbitrarily oriented crystals in 3D periodic simulation cells with applications to crystal–crystal interfaces, Computer Physics Communications (2016), http://dx.doi.org/10.1016/j.cpc.2016.07.007

requirement also places enormous constraints on translational-symmetry-preserving rotations of the underlying crystal in a given simulation cell. One generally *cannot* arbitrarily rotate a crystal in a simulation cell with 3D PBCs to orient some direction in the crystal along another direction in the lab frame while preserving translational symmetry. Such requirements complicate studies that involve oriented crystals and can make it incredibly difficult to simultaneously model two or more different oriented crystals that satisfy PBCs in a single simulation cell. This severely hinders simulation studies of many anisotropic properties, grain boundaries, and crystal–crystal interfaces between different polymorphs and materials.

Literature sources include some reports of 3D periodic cells containing oriented crystals [1,2,4–6] and (at least apparent) orthorhombic representations of monoclinic [28] and triclinic [12,28] crystals. We are also aware of one report [28] using cells containing two-dimensionally (2D) infinite interfaces with triclinic crystals and a recently developed method [39] for constructing interfaces in graphene. However, in most of these cases there is little to no discussion as to *how* the cells were constructed; where extensive discussion is given, the approach is not generalized for all Bravais lattices. These constructions appear to have been handled largely on a case-by-case basis.

In this report we develop a mathematical formalism and search-and-construction algorithms for the GCCM to facilitate the systematic construction of 3D periodic simulation cells containing arbitrarily oriented single crystals and thin films. The GCCM circumvents problematic (or impossible) crystal rotations by defining new simulation cells constructed by cutting inscribed crystals in a symmetry-preserving manner. As the GCCM is designed to preserve the translational-symmetry of all Bravais lattices, it can be applied to any crystal described by such a lattice irrespective of the complexity of the atomic or molecular structure or the symmetry of the space group. A simple formalism for defining constraints is employed that facilitates searches for possible orthorhombic representations of monoclinic and triclinic crystals and can be used to generate constituents of more complicated constructions, such as nanowires and nanoparticles. The GCCM formalism is readily extended to find commensurate 2D infinite crystal–crystal grain boundaries and interfaces that can be modeled in a single cell with 3D PBCs. Carefully ordering loop searches and application of constraints greatly reduces the computational complexity for finding commensurate crystal–crystal interfaces using the GCCM formalism and is necessary to make the calculation tractable.

The remainder of the article is organized as follows. The mathematical formalism and key algorithms for the GCCM are developed in Section 2, with constructions involving single crystals discussed in Section 2.1, extensions for 2D infinite crystal–crystal interfaces derived in Section 2.2, and strategies for constructing nanostructures with N-fold crystal–crystal interfaces presented in Section 2.3. Benefits and demonstrations of the GCCM for MD simulations are described in Section 3, namely computational advantages of using orthorhombic representations of low-symmetry crystals in Section 3.1, a comparison study of energetics of grain boundaries in a monoclinic molecular crystal in Section 3.2, and results from simulations of silver nanowires and icosahedral nanoparticles exhibiting five-fold twins in Section 3.3. Potential applications of the GCCM to systems including energetic materials, organic semiconductors, and pharmaceuticals are described with corresponding constructions in Section 4. Conclusions are drawn in Section 5. All of the GCCM software source code for constructing simulation cells of arbitrarily oriented single crystals and crystal–crystal interfaces is provided as Supplementary Material (see Appendix A).

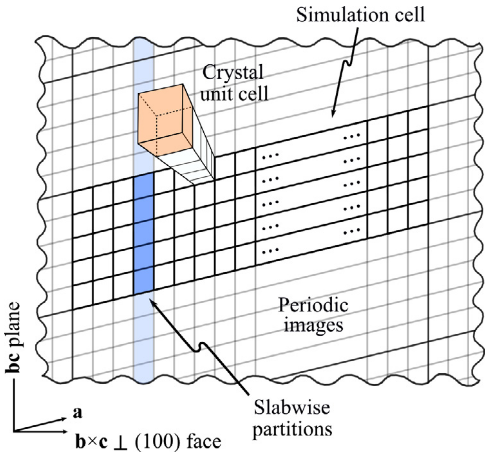

Fig. 1. A simulation cell constructed by translating the crystal unit cell has faces that coincide with the (100), (010), and (001) crystallographic faces. 2D periodic, 'infinite' slabwise partitions (see blue shaded region) can only be defined if the normal vector for the slab is parallel to the normal vector of one of the faces of the simulation cell, which in this case is also the normal of the (100) crystal face. Analogous slabwise partitions can be defined in this simulation cell with normal vectors parallel to the (010) and (001) face normal vectors. (For interpretation of the references to color in this figure legend, the reader is referred to the web version of this article.)

2. Generalized Crystal-Cutting Method (GCCM)

2.1. Constructing simulation cells of oriented single crystals

Here we derive a mathematical formalism for the GCCM for systematic construction of 3D periodic simulation cells of arbitrarily oriented single crystals. The GCCM comprises two algorithms. The first algorithm determines commensurate crystal cuts that preserve translational symmetry of the lattice and define the edges of new 3D periodic simulation cells. The second algorithm populates a chosen cell with atoms and/or molecules. These two algorithms serve as a basis to construct cells for many kinds of single-crystal simulations and for more complicated constructions such as crystal–crystal interfaces.

Consider a crystal with a Bravais lattice of arbitrary symmetry class with lattice vectors **a**, **b**, and **c** and an arbitrary set of basis atoms for the unit cell. The respective lattice vector lengths are a, b, and c and the angles between the lattice vectors are $\alpha\angle\mathbf{bc}$, $\beta\angle\mathbf{ac}$, and $\gamma\angle\mathbf{ab}$. Given 3D PBCs, simple unit cell translations can be used to trivially create simulation cells with surfaces normal to the crystal faces (100), (010), (001), $(\bar{1}00)$, $(0\bar{1}0)$, and $(00\bar{1})$. (Recall that the (ijk) and $(\overline{ijk})$ faces are equivalent for centrosymmetric crystals.) Fig. 1 shows one such simulation cell suitable for probing properties along the normal to the (100) face. It is clearly seen that the (100) face normal vector is exactly perpendicular to **b** and **c**, but is not parallel to **a** (*i.e.*, lattice direction [100]) for crystals with monoclinic or triclinic symmetry. A crystal face (ijk) normal vector is in general parallel to lattice direction $[ijk]$ only for cubic crystals.

A critical feature of the simulation cell construction in Fig. 1 is that the periodic boundaries allow for 'infinite' 2D slabwise partitions, highlighted by shading, whose normal vector is exactly parallel to the normal of the (100) face. Clearly, analogous slabs can be defined in this cell with normal vectors parallel to the normals of the (010) and (001) faces. It can also be seen that it is impossible to use this cell to define smooth-faced infinite 2D periodic slabs with different orientations, such as those with normal directions [100] or perpendicular to (110). However, defining infinite 2D slabs in the cell is desirable, or necessary, for many types of simulations. For instance, simulations of supported shock waves often use a 2D infinite rigid piston (or momentum mirror) with a normal vector

Please cite this article in press as: M.P. Kroonblawd, et al., A generalized crystal-cutting method for modeling arbitrarily oriented crystals in 3D periodic simulation cells with applications to crystal–crystal interfaces, Computer Physics Communications (2016), http://dx.doi.org/10.1016/j.cpc.2016.07.007

that is parallel to the shock direction [1,4,19], and simulations of 1D transport require 2D slabwise partitions with normal vectors parallel to the transport direction to impose or measure fluxes and gradients [3,7,24,29,30,40]. Similar requirements exist for simulations probing the directions transverse to the slab normal vector, such as for the calculation of a gamma-surface [41] on a slip plane [2,9]. The only requirement for slabwise partitioning of a 3D periodic simulation cell into 2D periodic slabs is that the normal vector of the slab be exactly parallel or antiparallel to the normal of a face of the *simulation cell*. One can probe an arbitrary direction **S** in a crystal provided that **S** is exactly parallel to the normal of one of the three unique faces of the simulation cell and that the simulation cell preserves the translational symmetry of the underlying crystal.

The first GCCM algorithm determines the possible geometries for new simulation cells that yield a face normal vector aligned with an arbitrary direction **S**. The new cells are in general triclinic and must be exactly commensurate with the underlying crystal structure. We define the edges for an arbitrary cell that satisfies the commensurability conditions as $\mathbf{x}_1$, $\mathbf{x}_2$, and $\mathbf{x}_3$, where

$$\mathbf{x}_j = m_j\mathbf{a} + n_j\mathbf{b} + p_j\mathbf{c}, \tag{1}$$

and m_j, n_j, and p_j are integers that will be determined later. (That is, the $\mathbf{x}_j$'s are all lattice vectors.) Thus, a particular cell is specified by the matrix $(\mathbf{x}_1, \mathbf{x}_2, \mathbf{x}_3)$, where the $\mathbf{x}_j$'s are Cartesian column vectors. Note that periodicity of a Bravais lattice with an arbitrary set of basis atoms or molecules is satisfied with edge vectors of the form given in Eq. (1), which can be seen for the 2D projection shown in Fig. 2. The simulation cell must have finite volume, thus the new edge vectors must satisfy $V = \mathbf{x}_1 \cdot (\mathbf{x}_2 \times \mathbf{x}_3) > 0$. We assume here and in all following discussion that $\mathbf{x}_1$, $\mathbf{x}_2$, and $\mathbf{x}_3$ comprise a right-handed basis. Expressing the cell edge vectors in the form given by Eq. (1) allows one to easily define geometrical constraints for $(\mathbf{x}_1, \mathbf{x}_2, \mathbf{x}_3)$ and requires only **S**, **a**, **b**, and **c** as input information. The form of the $\mathbf{x}_j$'s guarantees that translational symmetry is satisfied.

To construct simulation cells for determining a property along **S**, we first find vector pairs $(\mathbf{x}_1, \mathbf{x}_2)$ such that for each pair

$$\widehat{\mathbf{x}_1 \times \mathbf{x}_2} = \hat{\mathbf{S}}, \tag{2}$$

where $\hat{\mathbf{S}}$ and $\widehat{\mathbf{x}_1 \times \mathbf{x}_2}$ are unit vectors. It is through this constraint on $(\mathbf{x}_1, \mathbf{x}_2)$ that the normal of a simulation cell face is guaranteed to be exactly aligned with the **S** direction. The possible pairs $(\mathbf{x}_1, \mathbf{x}_2)$ can be identified in a simple and relatively inexpensive search that loops over values for the free parameters m_1, n_1, p_1, m_2, n_2, and p_2. It should be obvious that one is *not* guaranteed to find finite $m_1, \ldots, p_2$ that exactly satisfy Eq. (2). The set of pairs that satisfy or nearly satisfy Eq. (2) (within a user-specified scalar tolerance ϵ) can be efficiently identified by checking whether $\hat{\mathbf{S}} \cdot (\widehat{\mathbf{x}_1 \times \mathbf{x}_2}) \geq 1 - \epsilon$ for all possible combinations of $\mathbf{x}_1$ and $\mathbf{x}_2$ on some finite domain for $(m_1, \ldots, p_2)$. For the case $\epsilon \neq 0$, one has a simulation cell in which the face normal vector and **S** are misaligned by an angle that is at most $\theta = \cos^{-1}(1 - \epsilon)$, but where the crystal structure is exactly preserved and the discrepancy between these two directions can be known exactly. In this case one should treat $\widehat{\mathbf{x}_1 \times \mathbf{x}_2}$ as the aligned direction, not $\hat{\mathbf{S}}$. Having found $(\mathbf{x}_1, \mathbf{x}_2)$, one can choose any $\mathbf{x}_3$ that has form given by Eq. (1) provided $\hat{\mathbf{x}}_3 \cdot \hat{\mathbf{S}} \neq 0$.

New simulations cells $(\mathbf{x}_1, \mathbf{x}_2, \mathbf{x}_3)$ found by following the above approach are in general triclinic. One can identify orthorhombic cells among the set of all possible solutions by imposing the constraint

$$\mathbf{x}_1 \cdot \mathbf{x}_2 = 0, \tag{3}$$

during or after the initial search for $(\mathbf{x}_1, \mathbf{x}_2)$ pairs and imposing the constraint

$$\hat{\mathbf{x}}_3 \cdot \hat{\mathbf{S}} = 1, \tag{4}$$

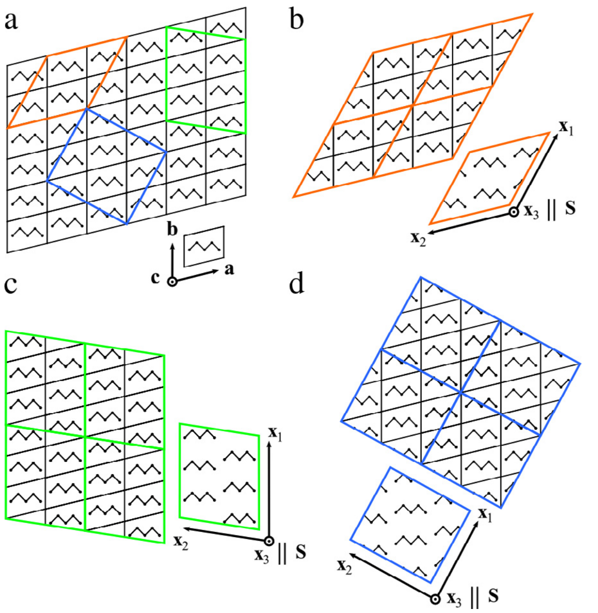

Fig. 2. Many different simulation cells can be constructed with a face normal vector parallel to **S**, which in this case is $\mathbf{S} = \mathbf{a} \times \mathbf{b}$ and points out of the page. The original crystal structure and unit cell are shown in (a) along with three new simulation cells that are commensurate with the lattice and highlighted with (b) orange, (c) green, and (d) blue edges. All three cells preserve the translational symmetry of the crystal, but the blue cell in (d) is the arguably the best for single-crystal simulations as it is the closest to orthorhombic symmetry. Note, however, that the crystals in these cells each have different faces aligned with the cell faces given by $\mathbf{x}_1 \times \mathbf{x}_3$ and $\mathbf{x}_2 \times \mathbf{x}_3$ and therefore have different 2D infinite slabwise partitions that can be defined analogous to those shown in Fig. 1. (For interpretation of the references to color in this figure legend, the reader is referred to the web version of this article.)

when searching for possible $\mathbf{x}_3$. One can also easily redefine the constraint in Eq. (3) to search for approximately rectangular transverse cross-sections within some tolerance angle ϵ' as $|\hat{\mathbf{x}}_1 \cdot \hat{\mathbf{x}}_2| < \cos(90^\circ - \epsilon')$ and similarly to search for approximately orthorhombic cells by modifying Eq. (4). Note that $\widehat{\mathbf{x}_1 \times \mathbf{x}_2}$ should be substituted for $\hat{\mathbf{S}}$ in Eq. (4) if these two vectors are not exactly parallel. Irrespective of finding a perfectly orthorhombic simulation cell, in choosing $\mathbf{x}_3$ one would likely seek to either find the minimum total cell volume, identified as $\mathbf{x}_1 \cdot (\mathbf{x}_2 \times \mathbf{x}_3) \rightarrow$ minimum, or the cell closest to orthorhombic geometry, identified as $\hat{\mathbf{x}}_1 \cdot \left(\hat{\mathbf{x}}_2 \times \hat{\mathbf{x}}_3\right) \rightarrow 1$, or a combination of these two criteria. Minimizing with respect to cell volume will generally *not* lead to a primitive unit cell for directions **S** that are not exactly parallel to one of the crystal faces (100), (010), or (001).

The initial search for commensurate pairs $(\mathbf{x}_1, \mathbf{x}_2)$ is by far the most computationally demanding step for a generalized implementation with loops over m, n, and p. The calculation scales as $\mathcal{O}(\Delta m^6)$ where Δm is the number of elements in the search domain for (m_1, m_2) and assuming $\Delta m = \Delta n = \Delta p$. The subsequent search for $\mathbf{x}_3$ is much cheaper, scaling approximately as $\mathcal{O}(\Delta m^3)$. Separating the searches for $(\mathbf{x}_1, \mathbf{x}_2)$ and $\mathbf{x}_3$ already drastically reduces the computational complexity from an $\mathcal{O}(\Delta m^9)$ maximum. Although $\mathcal{O}(\Delta m^6)$ may seem large, even serial searches that loop over the domain $-15 \leq m, n, p \leq 15$ (which corresponds to a maximum cross-sectional area up to approximately 15 × 15 square unit cells and $\Delta m = 31$) execute in less than a minute on a desktop computer. Obviously, the GCCM search algorithm is also embarrassingly parallel. The computational complexity can be reduced to $\mathcal{O}(\Delta m^4)$ if one only searches over those $(\mathbf{x}_1, \mathbf{x}_2)$ that lie exactly in the plane with normal vector **S**. Complexity reduction can be easily achieved for **S** parallel to the (100), (010), and (001) face normal vectors by respectively eliminating the loops over m, n, or p. Such

Please cite this article in press as: M.P. Kroonblawd, et al., A generalized crystal-cutting method for modeling arbitrarily oriented crystals in 3D periodic simulation cells with applications to crystal–crystal interfaces, Computer Physics Communications (2016), http://dx.doi.org/10.1016/j.cpc.2016.07.007

an approach is particularly advantageous when searching for orthorhombic representations of monoclinic and triclinic crystals. $\mathcal{O}(\Delta m^4)$ scaling can be achieved for arbitrary $\mathbf{S}$ using a two-step approach whereby one first finds a small oriented cell $(\mathbf{x}_1, \mathbf{x}_2, \mathbf{x}_3)$ through a general search over a limited (m, n, p) domain and then performs a second search over (m', n') for $(\mathbf{x}'_1, \mathbf{x}'_2)$ where $\mathbf{x}'_j = m'_j\mathbf{x}_1 + n'_j\mathbf{x}_2 + p'_j\mathbf{x}_3$. (Recall $\mathbf{x}_1$ and $\mathbf{x}_2$ lie in the plane with normal $\mathbf{S}$ by construction.) Many studies require a simulation cell that is longer along $\mathbf{S}$ than along either dimension of the cross-section. In these instances one can cheaply increase the search domain size for (m_3, n_3, p_3) relative to the domain for $(m_1, \dots, p_2)$ when attempting to find the cell that is closest to orthorhombic geometry.

The second GCCM algorithm automates the process of populating a chosen simulation cell $(\mathbf{x}_1, \mathbf{x}_2, \mathbf{x}_3)$ with constituent atoms or molecules. The approach is as follows: First, replicate the crystal through translations of the original unit cell over a domain twice as large as was covered in the original search. Second, rotate the crystal such that $\mathbf{x}_1$ is parallel to x, $\mathbf{x}_2$ is the in (x, y)-plane, and $\mathbf{x}_3$ is in the $+z$ half-space. Third, transform the rotated coordinates of the atoms in the crystal to fractional coordinates with respect to the aligned $(\mathbf{x}_1, \mathbf{x}_2, \mathbf{x}_3)$ simulation cell and populate the new cell with those atoms having fractional coordinates $(x_{\text{frac}}, y_{\text{frac}}, z_{\text{frac}}) \in (0, 1]$. Performing the intermediate rotation step is optional, but simplifies the transformation matrix to convert between fractional and Cartesian coordinates and conveniently aligns $\mathbf{S}$ to be exactly along $+z$. Because pairs of molecules that are equivalent under PBCs can be included along the edges of the cell with this approach due to finite numerical precision, a final inspection of the cell for such pairs using minimum-image conventions is often necessary. Sample programs to calculate edge vectors for simulation cells of oriented single crystals and to populate those cells using the above approach are provided as Supplementary Material (see Appendix A).

2.2. Constructing simulation cells for crystal–crystal interfaces

A straightforward extension of the GCCM formalism developed in Section 2.1 allows for easy specification of constraints necessary to construct fully 2D periodic crystal–crystal interfaces between Bravais-lattice crystals of arbitrary symmetry class in a simulation cell with 3D PBCs. Additional attention must be paid to the implementation details for searches and application of constraints as the computational complexity is significantly greater than for the single-crystal case. We concern ourselves here with the construction of an interface between two oriented crystals, which in general may correspond to the same material, two different polymorphs of the same chemical substance, or two completely different substances. One can easily extend the construction scheme to three or more different oriented crystals. Let the initial simulation cells for two separate oriented crystals with face normals aligned with user-specified directions $\mathbf{S}$ and $\mathbf{S}'$ be denoted as $(\mathbf{x}_1, \mathbf{x}_2, \mathbf{x}_3)$ and $(\mathbf{x}'_1, \mathbf{x}'_2, \mathbf{x}'_3)$, respectively. Following the conventions of Section 2.1, the face normal vectors given by $\mathbf{x}_1 \times \mathbf{x}_2$ and $\mathbf{x}'_1 \times \mathbf{x}'_2$ are respectively aligned with $\mathbf{S}$ and $\mathbf{S}'$. Define the angles between the cell edge vectors to be $\theta\angle\mathbf{x}_1\mathbf{x}_2$, $\phi\angle\mathbf{x}_1\mathbf{x}_3$, and $\psi\angle\mathbf{x}_2\mathbf{x}_3$ and similarly for θ', ϕ', and ψ'. Given these definitions, we specify two sets of constraints to construct an interface following the schematic shown in Fig. 3.

The first set of constraints forces commensurate crystal geometries at the interface cross-section. Starting from the possible pairs $(\mathbf{x}_1, \mathbf{x}_2)$ and $(\mathbf{x}'_1, \mathbf{x}'_2)$ that separately satisfy Eqs. (1) and (2), we require that

$$\begin{aligned} q|\mathbf{x}_1| &= q'|\mathbf{x}'_1|, \\ r|\mathbf{x}_2| &= r'|\mathbf{x}'_2|, \\ \theta &= \theta', \end{aligned} \tag{5}$$

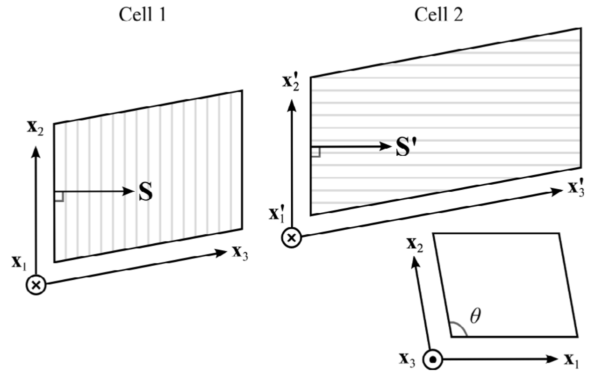

Fig. 3. Schematic for the construction of a 2D infinite crystal–crystal interface that can be inscribed in a single simulation cell. The formal mathematical constraints for this construction are given in Eqs. (5) and (6).

where q, q', r, and r' are integers equal to or greater than one and $|\mathbf{x}_j|$ denotes the magnitude of $\mathbf{x}_j$. The commensurate pairs satisfying these equations are denoted $(\mathbf{x}_1, \mathbf{x}_2, \mathbf{x}'_1, \mathbf{x}'_2)$, and can be found by looping over all unique combinations of $(\mathbf{x}_1, \mathbf{x}_2)$ and $(\mathbf{x}'_1, \mathbf{x}'_2)$ pairs. Setting q, q', r, and r' to unity simplifies the specification and computational complexity of the search. Unlike for the single crystal, there are also strict requirements for simultaneously choosing $\mathbf{x}_3$ and $\mathbf{x}'_3$, which form the second set of constraints. Having first found possible solutions for the cross-section $(\mathbf{x}_1, \mathbf{x}_2, \mathbf{x}'_1, \mathbf{x}'_2)$, we require that

$$\begin{aligned} \phi &= \phi', \\ \psi &= \psi', \end{aligned} \tag{6}$$

when choosing $\mathbf{x}_3$ and $\mathbf{x}'_3$ to form a complete solution $(\mathbf{x}_1, \mathbf{x}_2, \mathbf{x}_3, \mathbf{x}'_1, \mathbf{x}'_2, \mathbf{x}'_3)$ for the 2D periodic interface problem. It is not necessary that $|\mathbf{x}_3|$ and $|\mathbf{x}'_3|$ be equal within an integer multiple, but rather only that these two vectors form the same angles with the interface cross-section. As with the single-crystal constructions, user-defined tolerances for satisfying the constraints in Eqs. (5) and (6) can be applied, which corresponds to allowing for non-zero lattice strains.

The existence of a solution on a user-defined domain $(m_1, \dots, p_3)$ is by no means guaranteed and is governed entirely by the constituent crystal structure(s). However, a search-based approach does provide a feasible means to prove, by exhaustion, the non-existence of a solution for a particular case on some domain. Finite tolerances on the constraints in Eqs. (5) and (6) are often necessary to find any solutions $(\mathbf{x}_1, \mathbf{x}_2, \mathbf{x}_3, \mathbf{x}'_1, \mathbf{x}'_2, \mathbf{x}'_3)$. Minimum values for these tolerances can be chosen with respect to the uncertainty in the lattice parameters. The two oriented crystals are ultimately inscribed in a single simulation cell, which can be constructed using the average values computed for the constrained geometric parameters $\langle|\mathbf{x}_1|\rangle$, $\langle|\mathbf{x}_2|\rangle$, $\langle\theta\rangle$, $\langle\phi\rangle$, and $\langle\psi\rangle$ obtained from the $(\mathbf{x}_1, \mathbf{x}_2, \mathbf{x}_3)$ and $(\mathbf{x}'_1, \mathbf{x}'_2, \mathbf{x}'_3)$ cells. If this average cell is used, the necessary strains imposed separately on the crystals in $(\mathbf{x}_1, \mathbf{x}_2, \mathbf{x}_3)$ and $(\mathbf{x}'_1, \mathbf{x}'_2, \mathbf{x}'_3)$ are only half the difference between these cells, a fact that can be exploited when defining tolerances. The two crystal cells must be rotated so that the edge vectors $(\mathbf{x}_1, \mathbf{x}_2, \mathbf{x}_3)$ and $(\mathbf{x}'_1, \mathbf{x}'_2, \mathbf{x}'_3)$ coincide and can be populated using the same procedure described in Section 2.1.

In many cases, the number of solutions identified by the GCCM is overwhelmingly small compared to the total number of candidate ways to cut and join two crystals, the majority of which do not satisfy 3D PBCs. For instance, if the domain for m, n, and p is taken to be $-15 \le m, n, p \le 15$, then there are a total of $\mathcal{O}(\Delta m^{18}) \approx \mathcal{O}(10^{26})$ ways to cut and join two simulation cells. However, by carefully ordering searches and the application of constraints, the computational complexity of this algorithm can be greatly reduced.

Please cite this article in press as: M.P. Kroonblawd, et al., A generalized crystal-cutting method for modeling arbitrarily oriented crystals in 3D periodic simulation cells with applications to crystal–crystal interfaces, Computer Physics Communications (2016), http://dx.doi.org/10.1016/j.cpc.2016.07.007

In part one of the crystal–crystal interface search algorithm, the possible cross-sections $(\mathbf{x}_1, \mathbf{x}_2)$ and $(\mathbf{x}'_1, \mathbf{x}'_2)$ consistent with the user specified directions $\mathbf{S}$ and $\mathbf{S}'$ are identified in two separate searches that each scale as $\mathcal{O}(\Delta m^6)$. In our experience for polyatomic molecular crystals these searches might find at most $\mathcal{O}(10^3)$ to $\mathcal{O}(10^4)$ possibilities for each cross-section. It is reasonable to consider only those cross-sections for which θ and θ' are near 90°, where 'near' can be specified by the user, so that the final simulation cell is not excessively tilted. In part two, all permutations of the possible cross-sections are compared and only the commensurate pairs satisfying the constraints in Eq. (5) are kept. Often there are only a few dozen or hundred commensurate cross-section pairs, or even none. In the latter case the search domain $(m_1, \ldots, p_2)$ or tolerances should be increased. The third and final part is to find appropriate $\mathbf{x}_3$ and $\mathbf{x}'_3$ for the commensurate cross-sections, subject to the constraints in Eq. (6). As the search to find the best $\mathbf{x}_3$ and $\mathbf{x}'_3$ for each commensurate cross-section pair scales as $\mathcal{O}(\Delta m^6)$, this final part of the algorithm can be the most expensive in the event that many possible cross-sections pairs are identified. Here we take 'best' to mean those $\mathbf{x}_3$ and $\mathbf{x}'_3$ that lead to a final cell that is the closest to orthorhombic symmetry within tolerances for ϕ and ψ. To reduce the total computational cost of the algorithm, it is beneficial to perform this final search only for the best pairs $(\mathbf{x}_1, \mathbf{x}_2, \mathbf{x}'_1, \mathbf{x}'_2)$, with 'best' being reasonably defined as those cross-section pairs that are closest to being exactly commensurate $(|\mathbf{x}_1| - |\mathbf{x}'_1| \to 0, |\mathbf{x}_2| - |\mathbf{x}'_2| \to 0, \theta - \theta' \to 0)$ or closest to orthorhombic symmetry $(\theta, \theta' \to 90^\circ)$. A sample program to compute commensurate crystal–crystal interfaces is provided as Supplementary Material (see Appendix A).

It should be noted when constructing interfaces with the GCCM that the above constraints do not control the twist of one crystal with respect to the other. For a homophase interface, this can lead to a grain boundary with both a tilt and a twist [42]. If one is searching for a specific twist, appropriate constraints can defined and incorporated at relevant points in the general GCCM search routines. In our experience with low-symmetry materials, there are often only a few dozen or hundred possible interfaces identified by the GCCM, so it is likely not possible to exert a high degree of control on the twist for those materials on a practically tractable search domain.

2.3. Constructing N-fold crystal–crystal interfaces

The mathematical formalism developed in Section 2.1 can be further extended to provide a systematic means to construct high-symmetry defect structures, such as a five-fold twin, and low-dimensional nanostructures, such as nanowires or icosahedral quasi-nanospheres. Similar to the 2D periodic crystal–crystal interface construction in Section 2.2, the existence of solutions for a particular case is dependent on the underlying crystal symmetry, the constraints can be simply and easily expressed, and a search algorithm guarantees that all possible solutions that exist on a specified domain are found.

Fig. 4(a) shows a schematic cross-section of a nanostructure with a 2D N-fold crystal–crystal interface. Two possible structures that can be built using this schematic include a free-standing thin film (which could be later adsorbed to a 2D periodic substrate) and a nanowire constructed through translations along $\mathbf{x}_2$. For both constructions, a new cell $(\mathbf{x}_1, \mathbf{x}_2, \mathbf{x}_3)$, highlighted with gray shading, is found and the nanostructure generated by $N - 1$ rotations of this cell about the vector $\mathbf{x}_2$ by integer multiples of $\phi = 360^\circ/N$. One must first specify the two interface normal vectors $\mathbf{S}$ and $\mathbf{S}'$. Unlike for a 2D periodic interface (Section 2.2), $\mathbf{S}$ and $\mathbf{S}'$ cannot be chosen independently, but rather must intersect with (approximately) the same angle ϕ. The geometric constraints on the cell are

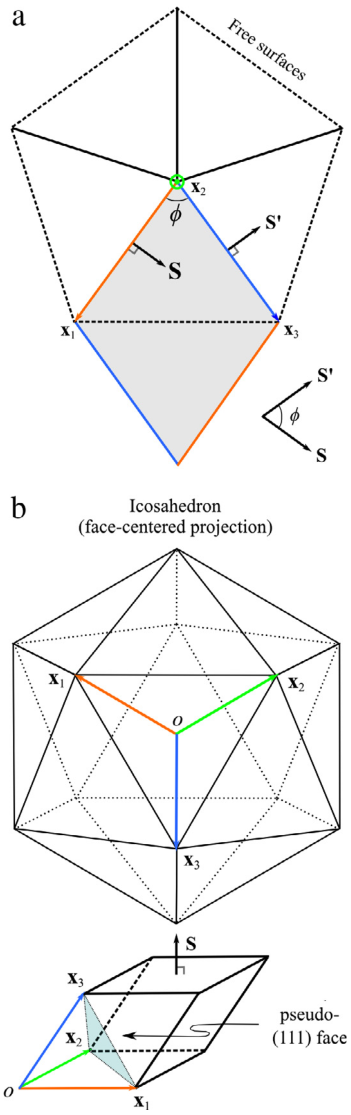

Fig. 4. Schematics for generating (a) an N-fold interface and (b) an icosahedral nanoparticle using the GCCM.

$$\begin{aligned} \widehat{\mathbf{x}_2 \times \mathbf{x}_1} &= \hat{\mathbf{S}}, \\ \widehat{\mathbf{x}_2 \times \mathbf{x}_3} &= \hat{\mathbf{S}}', \\ q|\mathbf{x}_1| &= r|\mathbf{x}_3|, \end{aligned} \tag{7}$$

where q and r are again integers equal to or greater than one. The cross-section can be made arbitrarily large by translating the cell along $\mathbf{x}_1$ and $\mathbf{x}_3$ prior to the N-fold rotation. One would also likely 'smooth' the edges of the cross-section by removing portions of the crystal outside some well-defined domain, such as the free surface indicated by dashed lines in the schematic.

A schematic for a particular icosahedral 3D analog to the 2D N-fold interface is shown in Fig. 4(b). An icosahedral nanoparticle has 20 faces and can be deconstructed into 20 separate (slightly irregular) tetrahedrons. To construct the icosahedron, we first find a parallelepiped-shaped cell with edge vectors $(\mathbf{x}_1, \mathbf{x}_2, \mathbf{x}_3)$ for a user-specified direction $\mathbf{S}$. We further require that

$$\begin{aligned} \mathbf{x}_1 \cdot \mathbf{x}_2 = \mathbf{x}_1 \cdot \mathbf{x}_3 = \mathbf{x}_2 \cdot \mathbf{x}_3 &= \cos(60^\circ), \\ q|\mathbf{x}_1| = r|\mathbf{x}_2| &= t|\mathbf{x}_3|, \end{aligned} \tag{8}$$

Please cite this article in press as: M.P. Kroonblawd, et al., A generalized crystal-cutting method for modeling arbitrarily oriented crystals in 3D periodic simulation cells with applications to crystal–crystal interfaces, Computer Physics Communications (2016), http://dx.doi.org/10.1016/j.cpc.2016.07.007

where q, r, and t are integers equal to or greater than one. The cell is then cut along the pseudo-(111) face corresponding to the ($\mathbf{x}_1$, $\mathbf{x}_2$, $\mathbf{x}_3$) edges, which is not necessarily the (111) crystal face. The 3D solid is obtained through rotations of the cut cell about the center of the icosahedron located at O.

It should be noted that the above GCCM constructions for the nanowire and nanoparticle examples are not perfect. Most nanostructures likely cannot be made outright from such simple geometric deconstructions. In the case of the nanowire, this is because two crystal faces are highly unlikely to have normal vectors that intersect at an angle that is exactly $\phi = 360^{\circ}/N$. For example, five-fold twins arise in face-centered cubic (FCC) metals because this angle is $\phi = 70.53^{\circ}$ [43], which is very close to the formal requirement $\phi = 72^{\circ}$. Likewise, an icosahedral nanoparticle cannot be constructed outright in this way because a regular icosahedron cannot be deconstructed into exactly regular tetrahedra (as is assumed for the constraints in Eq. (8)). Rather, the GCCM can be used to systematically obtain good starting configurations that are close to the final structures that subsequently result from either energy minimization or annealing.

3. Demonstrations

3.1. Advantages of orthorhombic simulation cells

Although many popular open-source MD simulation packages, such as DL_POLY CLASSIC [44], GROMACS [45], LAMMPS [46], and NAMD [47], support triclinic (parallelepiped-shaped) simulation cells, many of the algorithms implemented in a particular package only support orthorhombic cells. Algorithms for which triclinic support is often limited include full stress tensor (diagonal + off-diagonal terms) barostats, k-space solvers to handle long-range forces such as Coulomb, and support for heterogeneous computing architectures using accelerators such as graphics processing units (GPUs) or Intel® Many Integrated Core (MIC) cards. Whereas some algorithms, such as a barostat limited to diagonal terms of the stress tensor, are generally not recommended for use with MD simulations of any monoclinic or triclinic crystal, many of the above computational limitations can be overcome for these crystals provided they are modeled in an orthorhombic simulation cell. We demonstrate the advantages of orthorhombic simulation cells of low-symmetry crystals using LAMMPS. We chose LAMMPS over the alternatives in part because we are more familiar with it, but also because it supports all of the above algorithms (at least for orthorhombic cells). In particular, as of this writing, NAMD lacks support for full stress tensor barostats, and while DL_POLY CLASSIC has a rich feature set, orthorhombic cells for low-symmetry materials can be larger than the approximate 30,000-atom scaling limit.

As a test case we considered two simulation cells containing the monoclinic crystal β-HMX (β-octahydro-1,3,5,7-tetranitro-1,3,5,7-tetrazocine), modeled using a variant of the established flexible-molecule force field developed for HMX by Smith and Bharadwaj [48]. Both simulation cells were constructed using the average lattice parameters, which are $a = 6.57_9$ Å, $b = 10.4_5$ Å, $c = 7.68_3$ Å, $\alpha = 89.9^{\circ}_{9}$, $\beta = 98.6^{\circ}_{7}$, and $\gamma = 90.0^{\circ}_{0}$, that were obtained from the last 50 ps of a 250 ps (298 K, 1 atm) isobaric–isothermal (NPT) MD simulation. The first simulation cell was explicitly monoclinic and constructed by simple unit cell translations to yield a $23\mathbf{a} \times 10\mathbf{b} \times 20\mathbf{c}$ simulation cell with edge lengths 151 Å × 105 Å × 154 Å. The second simulation cell was exactly orthorhombic within the uncertainty of the lattice parameters, was constructed using the method in Section 2.1 with $\mathbf{S}$ equal to the (010) face normal vector, and had edge lengths 147 Å × 105 Å × 156 Å. Both simulation cells contained 9200 molecules. Substantially smaller orthorhombic cells containing ≈100 molecules were identified in our search, but we chose the larger one to eliminate potential finite-volume effects in the comparisons below.

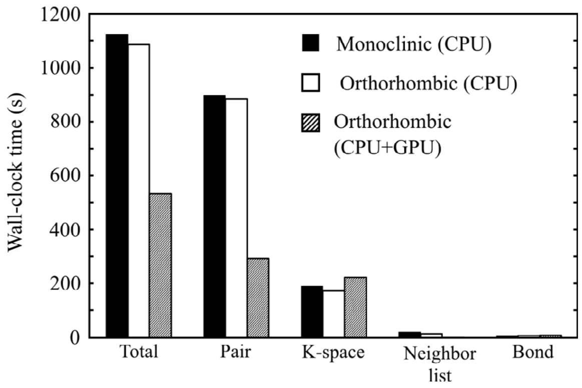

Fig. 5. Average timing data for three β-HMX MD simulation cases. The timing components are, from left to right, the total simulation time, the calculation of real-space non-bonded pairwise interactions, the k-space charge and force interpolations and fast Fourier transforms, the neighbor-list build time, and the time to compute the 2-, 3-, and 4-body bonded interactions. Contributions from all other simulation components had shorter timings than those shown in the figure.

The HMX force field consists of harmonic and truncated cosine series functions for the various two-, three-, and four-body covalent potentials. Non-bonded interactions, described using Buckingham (exp-6) plus Coulomb form, are included between atoms belonging to different molecules and between atoms separated by three or more covalent bonds in the same molecule. The only difference between the original parameterization of the HMX force field by Smith and Bharadwaj [48] and that used here is the values for two of the harmonic bond stretching force constants in $U_{\mathrm{bond}} = 0.5K(r - r_{\mathrm{o}})^2$, which are $K_{\mathrm{NO}} = 1120.0$ kcal mol^{-1} Å^{-2} for the N–O bonds and $K_{\mathrm{CH}} = 680.1$ kcal mol^{-1} Å^{-2} for the C–H bonds. These force constants were re-parameterized to better reproduce experimental vibrational spectra of HMX compared to the original parameterization and will be discussed more extensively in a subsequent publication. The dispersion and Coulombic terms were truncated at a real-space cutoff of 15 Å and the Coulombic interactions were calculated beyond the cutoff using the particle–particle particle-mesh [49] (PPPM) k-space method with a grid density of one grid point per Ångström. As LAMMPS performs the k-space calculation using the circumscribing orthorhombic cell, simulations with the monoclinic cell had more PPPM mesh points than did the simulations with the orthorhombic simulation cell. The corresponding ratio of the total number of mesh points was 1.145:1.

Timing data were collected from short 1000-timestep isochoric–isoergic (NVE) MD simulations of β-HMX using the monoclinic and orthorhombic simulation cells and the default integration timestep of 1.0 fs. The results are shown in Fig. 5. All simulations were performed on the same compute node, which is equipped with two hexa-core Intel® Xeon® E5-2620 CPUs and a single NVIDIA® Tesla® K40 GPU accelerator, and with the same version of LAMMPS built with the optional GPU package [50–52]. Three cases were considered: (1) the monoclinic cell run only on the CPUs; (2) the orthorhombic cell run only on the CPUs; and (3) the orthorhombic cell run on the CPUs, but with real-space non-bonded pairwise (Pair) interaction calculations, neighbor-list builds, and k-space charge/force interpolations offloaded to the GPU. The GPU package in LAMMPS currently does not support GPU acceleration for neighbor-list builds and PPPM k-space computations for monoclinic or triclinic simulation cells. Therefore, fully accelerated GPU-enabled LAMMPS simulations for β-HMX are only made possible by finding an equivalent explicit orthorhombic cell. Five separate instances of the same simulation were run for each

Please cite this article in press as: M.P. Kroonblawd, et al., A generalized crystal-cutting method for modeling arbitrarily oriented crystals in 3D periodic simulation cells with applications to crystal–crystal interfaces, Computer Physics Communications (2016), http://dx.doi.org/10.1016/j.cpc.2016.07.007

Table 1
Simulation cell details and predicted energy change per unit area (ΔU) for the formation of $(011)|(ijk)$ GBs.

GB type	ΔU (mJ m^{-2})	$\lvert\mathbf{x}_1\rvert$ (Å)	$\lvert\mathbf{x}_2\rvert$ (Å)	$\lvert\mathbf{x}_3\rvert$ (Å)	$\lvert\mathbf{x}'_3\rvert$ (Å)	Vacuum region length along $\mathbf{x}_3$ (Å)
$(011)\lvert(110)$	−186.6	81.81	61.98	103.06	127.72	70.00
$(011)\lvert(10\bar{1})$	−175.7	102.37	71.90	122.10	112.81	66.74
$(011)\lvert(010)$	−171.9	77.62	52.71	144.81	127.80	60.02
$(011)\lvert(11\bar{1})$	−80.8	50.33	111.43	123.20	105.89	67.01
$(011)\lvert(011)$	−373.0	50.33	111.43	123.20	123.20	67.78
(011)	−372.9	50.33	111.43	246.40	–	67.78

case and the relative run-to-run deviations in timings for each component were found to be within 1.0%, except for the k-space timings, for which the deviations were all within 7.0%.

The GPU-enabled simulation for the orthorhombic cell, which was obtained using the GCCM, exhibits a 52% reduction in wall-clock time compared to the simulation using the original monoclinic cell. The biggest contributor to this reduction is a threefold reduction in pairwise interaction calculation time. While it is not a large component of the total simulation time, the neighbor-list build time is reduced by over 99%. The k-space calculation time exhibits a modest increase that is likely due to communications overhead from splitting the fast Fourier transforms (performed on the CPU) and the charge/force interpolations (performed on the GPU). Smaller gains are realized when comparing the orthorhombic and monoclinic simulations performed only on the CPUs. This can be attributed to requiring a smaller PPPM mesh for the orthorhombic case. These speedups obtained here are likely relatively modest compared to what would be obtained for many other monoclinic and triclinic crystals, as computational efficiency generally decreases with increasing tilt of the simulation cell and the Smith Bharadwaj force field predicts that the monoclinic angle for β-HMX is only 98.68° (in the $P2_1/n$ space group).

3.2. Relative stability of Grain boundaries in β-HMX

As a demonstration of the GCCM for constructing crystal–crystal interfaces in low-symmetry molecular crystals, we investigate the relative stability of grain boundaries (GBs) in β-HMX using molecular dynamics/statics simulations in conjunction with the same HMX force field used in Section 3.1. The crystal surfaces used for constructing the GB were chosen based on recent experimental observations [53] of crystal habits and morphologies of β-HMX grown from acetone. Ranked morphological importance of the five most prominent crystallographic faces was given [53] as $(011) > (110) > (010) > (10\bar{1}) > (11\bar{1})$. Therefore, as a preliminary investigation, we study the relative stability of four different GBs, namely the (110), (010), $(10\bar{1})$, and $(11\bar{1})$ faces in contact with the (011) face. We denote these separate cases as $(011)|(110)$, $(011)|(010)$, $(011)|(10\bar{1})$, and $(011)|(11\bar{1})$. Note that β-HMX crystal is centrosymmetric, therefore the (ijk) and $(\bar{i}\bar{j}\bar{k})$ faces are equivalent.

3D periodic simulation cells containing commensurate β-HMX GBs were constructed using the procedures outlined in Section 2.2 with lattice parameters predicted by the HMX force field at (77 K, 1 atm). Lattice parameters were obtained from the final 50 ps of an NPT simulation in which an equilibrated simulation cell of β-HMX was first cooled from (298 K, 1 atm) to (77 K, 1 atm) at a rate of 0.442 K ps^{-1} and then held at (77 K, 1 atm) for an additional 250 ps. The average (77 K, 1 atm) lattice parameters are $a = 6.53_9$ Å, $b = 10.26_9$ Å, $c = 7.61_4$ Å, $\alpha = 90.0^{\circ}_{0}$, $\beta = 98.6^{\circ}_{6}$, and $\gamma = 90.0^{\circ}_{0}$. Starting configurations for the GBs were created by placing commensurate pairs of 2D periodic free-standing thin films (grains) into triclinic simulation cells that were constructed using the average values for the constrained geometric parameters $\langle|\mathbf{x}_1|\rangle$, $\langle|\mathbf{x}_2|\rangle$, $\langle\theta\rangle$, $\langle\phi\rangle$, and $\langle\psi\rangle$. The maximum relative change applied to any simulation cell parameter to make the individual grains commensurate was at most 0.1%. Use of the standard PPPM k-space method requires 3D PBCs, so a vacuum region was added in the $\mathbf{x}_3$ direction to simulate a free-standing thin-film bilayer consisting of a GB sandwiched between two exposed crystallographic faces. All simulation cell dimensions are given in Table 1. The initial distance between the individual grains at the GB interface plane corresponded to the potential energy (PE) minimum for the unrelaxed configuration with the outer surfaces exposed to vacuum. Each configuration thus obtained was then relaxed with fixed cell parameters using the 'FIRE' damped dynamics minimizer [54] until the final 'temperature' of the relaxed configuration was less than 2×10^{-5} K.

As a metric to predict the stability of the different GBs, we define the energy change per unit area for the formation of a GB as

$$\Delta U^{(011)|(ijk)} = \frac{U^{(011)|(ijk)} - U^{(011)} - U^{(ijk)}}{A^{(011)|(ijk)}}. \tag{9}$$

Here, $U^{(011)|(ijk)}$ is the total PE of the relaxed free-standing thin-film bilayer containing the $(011)|(ijk)$ GB, with $(0\bar{1}\bar{1})$ and $(\bar{i}\bar{j}\bar{k})$ outer free surfaces exposed to vacuum; the $U^{(ijk)}$ are respectively the total PEs of the relaxed single-component free-standing thin films with (ijk) and $(\bar{i}\bar{j}\bar{k})$ surfaces exposed to vacuum; and $A^{(011)|(ijk)}$ is the area of the GB given by $|\mathbf{x}_1 \times \mathbf{x}_2|$ (or equivalently $|\mathbf{x}'_1 \times \mathbf{x}'_2|$). Formation of a GB is thermodynamically favored compared to having two free-standing thin films if $\Delta U < 0$. Therefore, the signed values of ΔU can be used to predict and rank the relative stabilities of the GBs. Predicted values for ΔU are given in Table 1, from which it can be inferred that the stabilities of the GBs rank as $(011)|(110) > (011)|(10\bar{1}) > (011)|(010) > (011)|(11\bar{1})$. We also include results for two control calculations, denoted as $(011)|(011)$ and (011). The $(011)|(011)$ system is simply a special case of a 'GB' for which $(ijk) = (011)$ with no tilt or twist. The (011) case corresponds to a single free-standing thin film of the same dimensions as $(011)|(011)$, with the outer (011) and $(0\bar{1}\bar{1})$ faces exposed to vacuum as for the GBs. Very close correspondence between the $\Delta U^{(011)|(011)}$ and $\Delta U^{(011)}$ cases was obtained and establishes confidence in our simulation protocol. It can be seen that $\Delta U^{(011)|(011)} \ll \Delta U^{(011)|(ijk)}$, which implies that a free-standing thin film with exposed (011) outer surfaces and without a GB is considerably more stable than the similarly sized thin films with GBs.

Fig. 6(a) shows the average per-atom PE and the average pressure $P = -\frac{1}{3}\mathrm{Tr}(\boldsymbol{\sigma})$, where $\boldsymbol{\sigma}$ is the stress tensor, for the relaxed GB configurations as functions of the relative z coordinate, which is exactly perpendicular to the GB. The z coordinate for each GB case is shifted so that the location of the GB is at zero and is scaled so that the system length (excluding vacuum) is unity. We define the GB location as the midpoint of the z-projection of the line joining the nearest molecular center-of-mass positions in the two grains in the unrelaxed configuration. The locally averaged PE of each atom was calculated from the per-atom PEs obtained from LAMMPS by averaging over the surrounding spherical volume

Please cite this article in press as: M.P. Kroonblawd, et al., A generalized crystal-cutting method for modeling arbitrarily oriented crystals in 3D periodic simulation cells with applications to crystal–crystal interfaces, Computer Physics Communications (2016), http://dx.doi.org/10.1016/j.cpc.2016.07.007

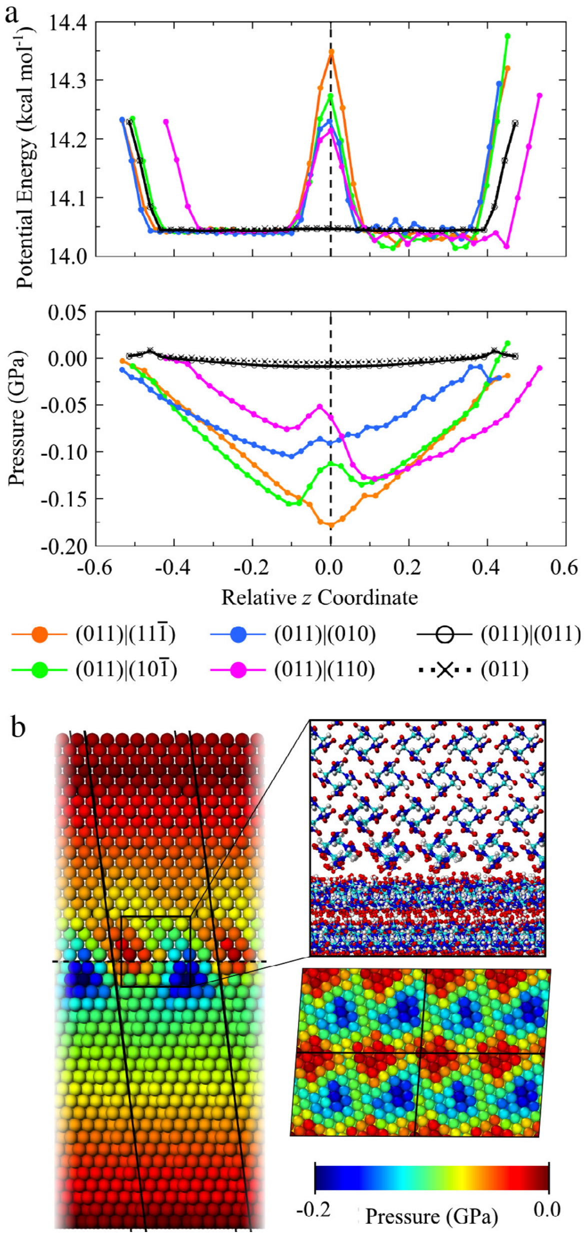

Fig. 6. (a) Averaged per-atom potential energy and averaged pressure in relaxed configurations of (011)|(*ijk*) GBs as a function of the relative *z* coordinate. (b) Relaxed configuration of the (011)|(010) GB with molecular centers of mass colored according to their locally averaged pressure. Top and bottom insets to panel (b) respectively show the atomic details and the locally averaged pressures for molecular centers of mass on the (011) face of the GB for the relaxed configuration. (For interpretation of the references to color in this figure legend, the reader is referred to the web version of this article.)

within a 15 Å radial cutoff. The average per-atom PE was then computed as a function of z by taking the arithmetic mean of the locally averaged atomic PEs of atoms assigned to 6 Å wide bins along the z-direction based on their atomic coordinates. The same local averaging scheme was used for calculation of the pressure, for which the volume of a sphere of radius 15 Å was used to normalize the averaged per-atom pressure, followed by binwise averaging. We also include results from the (011)|(011) and (011) cases for comparison to the results from the four GB simulations.

Fig. 6(a) clearly shows excess per-atom PE at the free surfaces and at the GB. The GBs are ordered according to increasing average per-atom PE at the GB (*i.e.*, at $z = 0$) as (011)|(110) < (011)|(010) < (011)|(10$\bar{1}$) < (011)|(11$\bar{1}$), which is in approximate agreement with the relative stability predicted using Eq. (9). We note that this ranking order for the (011)|(010) and (011)|(10$\bar{1}$) GBs is opposite to that predicted by Eq. (9), but that the predicted $\Delta U^{(011)|(ijk)}$ for those two cases are quite similar. The same ordering as for the per-atom PE is obtained for the average pressure at the GB, with the (011)|(11$\bar{1}$) case having the largest (most negative) value.

As a representative case, the relaxed (011)|(010) GB is studied in greater detail in Fig. 6(b). (The results in Fig. 6(b) and all subsequent figures were created using Visual Molecular Dynamics [55] (VMD) and the Open Visualization Tool [56] (OVITO) software packages.) The left-hand panel contains a snapshot of molecular centers of mass colored by locally averaged pressure and the smaller 'inset' panels to the right show an atomically detailed rendering across the interface (top) and locally averaged pressure for molecules in the (011) face of the GB (bottom). Periodic boundaries of the simulation cell are shown as solid lines. The predicted pressure distribution has a complicated pattern, with alternating regions of high and low pressure. This stands in contrast to the more homogeneous pressure distributions that were predicted for the other relaxed GBs investigated.

Interestingly, for all cases in panel (a) the average per-atom PE relaxes to a 'bulk' value at distances less than ≈15 Å from the GB, whereas the pressure does not. This indicates that long-ranged stress fields exist at these GBs. The apparent, but small, 'noise' in the average PE may be due to finite-size effects that result from interaction between the free surface and the GB. We note that the pressure is only slightly tensile for the (011)|(011) and (011) cases, as compared to the cases with GBs. This suggests that the long-ranged stress fields arise solely from the presence of the GB. In addition, there is near perfect correspondence between (011)|(011) and (011) cases for the average per-atom PE and pressure; while this establishes confidence in our simulation protocol, further investigation would be required to quantify the sensitivity of these preliminary predictions to system size and other simulation parameters.

3.3. Silver nanostructures

Five-fold twins have attracted extensive interest due to their unique properties since they were first observed in 1957 [57] and have been found in a variety of nanostructures including nanowires and nanorods [58], nanoparticles [14,15], and nanocrystalline metals and alloys [59]. Experimental studies of five-fold twinned nanowires (FTNWs) have revealed that the presence of the intrinsic five-fold axis alters many properties compared to the bulk, such as enhancing the yield strength [16,60] and elastic modulus [17] and inducing coiling motion [61]. Symmetrical icosahedral and truncated icosahedral nanoparticles with inner five-fold twins are also routinely recovered in experiments [14,62] and can spontaneously form in MD simulations [14,63]. Recent simulation studies predict that hex-conjoint five-fold twins can form in bent FTNWs before dynamic failure occurs [19] and that symmetrical quasi-icosahedral structures, which have configurations that are similar to icosahedral nanoparticles, can form in several kinds of FTNWs under dynamic tensile loading [18]. We show here how the GCCM can be used to easily construct nanostructures with intrinsic five-fold twins, such as FTNWs and icosahedral nanoparticles, which facilitates preparation of model systems for subsequent atomic simulations.

Starting configurations for a silver FTNW and icosahedral nanoparticle were prepared using the GCCM and the construction procedures outlined in Section 2.3. Silver crystallizes in a FCC structure with lattice constant $a = 4.09$ Å. We obtained the base cell $(\mathbf{x}_1, \mathbf{x}_2, \mathbf{x}_3)$ for the FTNW construction (see Fig. 4(a) schematic) from the single-crystal version of the GCCM by adding the additional constraints in Eq. (7) to the loop over possible $\mathbf{x}_3$ and setting $\mathbf{S} = [111]$ and $\mathbf{S}' = [1\bar{1}1]$. The cell edge lengths were

Please cite this article in press as: M.P. Kroonblawd, et al., A generalized crystal-cutting method for modeling arbitrarily oriented crystals in 3D periodic simulation cells with applications to crystal–crystal interfaces, Computer Physics Communications (2016), http://dx.doi.org/10.1016/j.cpc.2016.07.007

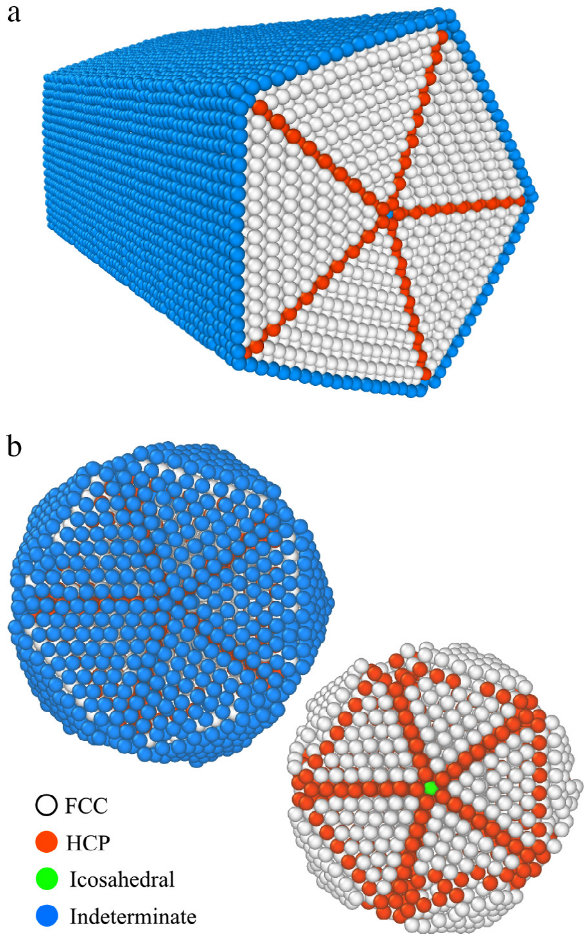

Fig. 7. Thermalized configurations of (a) a five-fold twinned Ag nanowire (FTNW) and (b) an icosahedral Ag nanoparticle obtained from starting configurations generated using the GCCM. Atoms are colored based on local configurations determined using common neighbor analysis and are white for FCC, orange for hexagonal close-packed (HCP), green for icosahedral, and blue for indeterminate local environments. The right nanoparticle in (b) is the same as the left nanoparticle, but with the blue indeterminate atoms removed to show the twin boundaries more clearly. The orange HCP atoms are on the twin boundaries and the green icosahedral atom is at the very center of the nanoparticle. (For interpretation of the references to color in this figure legend, the reader is referred to the web version of this article.)

$|\mathbf{x}_1| = 20a$, $|\mathbf{x}_2| = 10a$, and $|\mathbf{x}_3| = 20a$, and a triangular prismatic subsection was cut from the cell as shown in the schematic. The starting configuration for the FTNW was generated by rotating the triangular prismatic subsection about the $\mathbf{x}_2$ axis, which in this case is along $\langle 110 \rangle$, and removing the additional atoms generated by the rotation that overlap at the center. The FTNW was placed in a 3D periodic simulation cell with a large vacuum region in the transverse dimensions (*i.e.*, the $\mathbf{x}_1$-$\mathbf{x}_3$ plane) and the longitudinal dimension was set to $\mathbf{x}_2 = 10a$. The base cell for the icosahedral nanoparticle (see Fig. 4(b) schematic) was obtained by a similarly modified version of the GCCM that includes the constraints in Eq. (8) with $\mathbf{S} = [111]$. The cell edge lengths were $|\mathbf{x}_1| = |\mathbf{x}_2| = |\mathbf{x}_3| = 11a$, which leads to a nanoparticle with 10 'shells' surrounding the single central atom, and a tetrahedron was cut from this cell as shown in the schematic. The icosahedron was generated by first obtaining the 'top half' through rotations of the tetrahedron about the central atom at the origin and then inverting this top half though the origin to obtain the bottom half. Duplicates of atoms that form the twin boundaries were removed as were all duplicate central atoms. The resulting pseudo-icosahedron was placed in a 3D periodic simulation cell that was sufficiently large to avoid any self-interactions.

The starting nanostructure configurations were thermalized using NVT MD simulations performed with LAMMPS and are shown in Fig. 7. A Nosé-Hoover thermostat [64,65] was used to establish and maintain the system temperature at 298 K and the trajectories were integrated using a 1 fs time step. The embedded-atom-method (EAM) potential developed by Daw and Baskes [66] with the parameters from Foiles et al. [67] was used to describe the interatomic interactions. Stable FTNW and icosahedral nanoparticle configurations were obtained from the starting configurations after 10 ps and 50 ps of NVT integration, respectively. In the case of the icosahedron, the required simulation time here is significantly lower than the 7 ns simulations previously used to obtain a similar particle from the melt [63]. As can be seen in Fig. 7(a), the thermalized FTNW exhibits five twin boundaries, each consisting of a single layer of atoms in a hexagonal close-packed (HCP) configuration, that converge to a shared center axis (along $\mathbf{x}_2$) that forms the intrinsic five-fold twinned structure throughout the nanowire. Fig. 7(b) shows the icosahedral nanoparticle surface, which exhibits 30 twin boundaries that 'divide' the surface into 20 faces. There are 12 five-fold twin centers that start at the central atom and terminate at the 12 vertices on the surface; these divide the solid into 20 approximately regular tetrahedrons. These well-defined five-fold twinned structures clearly demonstrate that GCCM-based constructions can serve as reasonable starting configurations for simulating FTNWs and icosahedral nanoparticles. We anticipate that other nanostructures can also be obtained through a similar approach and can drastically reduce the wall-clock time required compared to obtaining nanostructure configurations through simulated annealing and quenching processes [63] that can be kinetically hindered.

4. Potential applications

There are many problems in materials science that can be addressed using simulation cells systematically constructed using the GCCM. Here we highlight three additional topic areas not covered in Section 3, namely cocrystals, organic semiconductors, and pharmaceuticals. These examples are given without corresponding simulations and are included merely to emphasize how the GCCM could be useful to a wide range of applications. In particular, it should be noted that the examples of crystal grain boundaries and crystal–crystal interfaces below were constructed using experimental lattice parameters and the configurations are neither thermalized nor energy-minimized.

Recent reactive MD studies predict [8] that some cocrystals of energetic materials, such as cocrystals of TNT (2,4,6-trinitrotoluene) and CL-20 (2,4,6,8,10,12-hexanitro-2,4,6,8,10,12-hexaazaisowurtzitane), may have decreased sensitivity relative to their 'pure' constituents. In addition to decreased sensitivity, the possibility for significant anisotropy in the mechanical and thermal response of energetic cocrystals is perhaps greater than for most single-component crystals as cocrystals often exhibit complicated layered packing motifs [35,36]. Fig. 8(a) shows nearly orthorhombic simulation cells for two oriented crystals of another (monoclinic) energetic cocrystal comprised of CL-20 and HMX (2:1 ratio) that were constructed using the GCCM with the lattice parameters determined by Bolton et al. [36]. It is clearly seen that the orientation of the HMX molecules (in blue) relative to the surface-normal direction **S** differs considerably for **S** perpendicular to the (001) and (110) faces. It is natural to question whether this orientational difference, taken together with the difference in angle between the HMX layers and the shock direction, could lead to significant anisotropy in shock response and sensitivity.

Organic molecular semiconducting materials, such as the layered triclinic molecular crystal pentacene, have received significant attention for their potential use in electronics applications

Please cite this article in press as: M.P. Kroonblawd, et al., A generalized crystal-cutting method for modeling arbitrarily oriented crystals in 3D periodic simulation cells with applications to crystal–crystal interfaces, Computer Physics Communications (2016), http://dx.doi.org/10.1016/j.cpc.2016.07.007

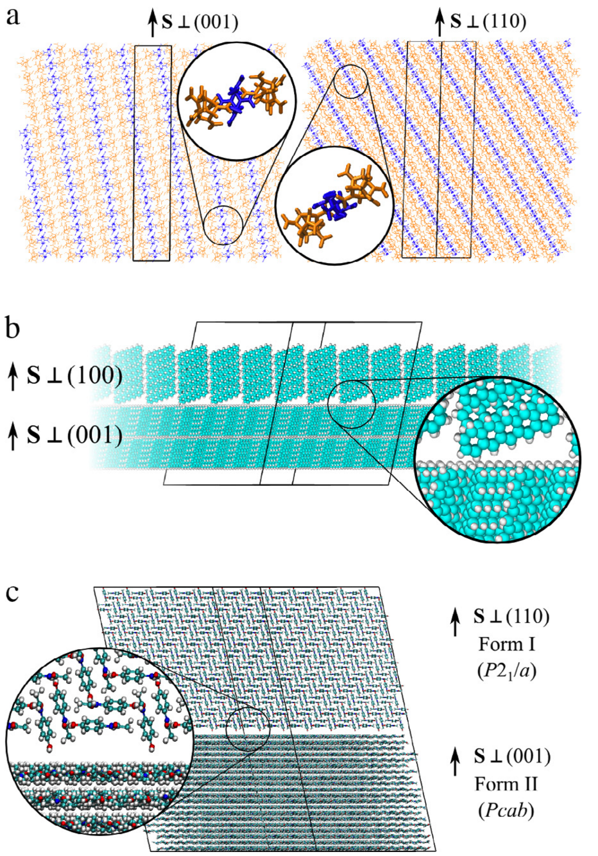

Fig. 8. Example systems prepared using the GCCM including: (a) oriented 2:1 cocrystals of CL-20 (orange) and HMX (blue); (b) an (001)|(100) grain boundary between pentacene thin films; (c) a heterophase interface between the orthorhombic and monoclinic polymorphs of acetaminophen. In all cases, the primary 3D periodic simulation cell is drawn with black lines and in most instances the cell is tilted so that the faces are not in the plane of the page. Periodic images are shown in (a) and (b), but not in (c). Because the pentacene and monoclinic acetaminophen polymorphs respectively shown in (b) and (c) are centrosymmetric, the (100) and $(\bar{1}00)$ faces are equivalent as are the (110) and $(\bar{1}\bar{1}0)$ faces. (For interpretation of the references to color in this figure legend, the reader is referred to the web version of this article.)

[3,11,13,26,37,38,68–71]. Pentacene exhibits multiple polymorphs characterized by differences in the separation distance between the molecule-thick layers that stack along the normal to the (001) crystal face. Polymorphic expression in pentacene is sensitive to the manner in which the crystals are grown and whether the crystal is adsorbed to a substrate [37,38]. Defects, such as grain boundaries, can develop [70,71] and alter the electrical [26,69] and potentially the thermomechanical properties compared to perfect crystal. Constructing pentacene grain boundaries and pentacene–substrate interfaces in 3D periodic simulation cells using the GCCM facilitates use of standard MD methods to assess the influence of these interfaces on transport properties without additional effects due to exposed edges. Fig. 8(b) shows an idealized 2D infinite grain boundary between the (001) and (100) faces in oriented pentacene thin films constructed using the GCCM with the techniques in Section 2.2 and the lattice parameters determined at 293 K by Mattheus et al. [37]. Expression of these two faces is predicted to be energetically favorable [11,13], so it is conceivable that this or other grain boundaries may develop in real crystals. Both thin films in Fig. 8(b) were extracted from larger cells with identical transverse dimensions, but longer extents along $\mathbf{x}_3$ and $\mathbf{x}'_3$, and were then inscribed in a single cell that satisfies the constraints in Eqs. (5) and (6). This example highlights the generalized nature of the GCCM in that it can find possible interfaces even between two triclinic crystals and can likewise be used to construct heterophase interfaces between pentacene and other substrates of arbitrary symmetry class.

Acetaminophen, one of the most widely used analgesic and antipyretic drugs, has two well characterized polymorphs, namely form I (monoclinic, spacegroup $P2_1/a$) [32] and form II (orthorhombic, spacegroup $Pcab$) [31]. Although these two polymorphs are known not to differ in their bio-availability, the metastable form II polymorph of acetaminophen has better compaction properties compared to the stable form I polymorph, and is therefore better suited for industrial manufacturing of tablets [72]. Differences in their compaction properties arise from the nature of crystal packing, where the parallel, hydrogen-bonded molecular layers in the form II polymorph facilitate plastic deformation compared to the corrugated molecular layers in the form I polymorph. Fig. 8(c) shows a 3D periodic simulation supercell with an idealized heterophase interface between the (110) plane of the form I polymorph and the (001) plane of the form II polymorph, constructed using the GCCM. The individual oriented crystals were constructed using experimental lattice parameters and atomic fractional coordinates [31,32]. Interface structures such as these, between expressed crystal faces of the two polymorphs, possibly develop during transitions from form II to form I during storage of tablets [73] or during growth of polymorphic nuclei in evaporative deposition of thin films [74]. This example illustrates how the GCCM method can be used to construct 3D periodic simulation cells to investigate the properties of heterophase interfaces between low-symmetry polymorphs of molecular crystals such as those used as active pharmaceutical ingredients.

5. Conclusions

In this report we develop and implement a Generalized Crystal-Cutting Method (GCCM) for the systematic construction of three-dimensionally periodic simulation cells containing arbitrarily oriented single crystals and two-dimensionally infinite crystal–crystal interfaces. A simple mathematical formalism is used to conveniently express constraints on cut single-crystal geometries and is readily extended to specify constraints for constructing crystal–crystal homophase- and heterophase interfaces. The approach is generalized to include all Bravais lattices and so can be applied to complicated molecular crystals and materials that crystallize in low-symmetry systems. Search algorithms are implemented to find possible solutions for commensurate crystal cuts and an algorithm for populating the resulting simulation cells with constituent atoms and molecules is outlined. The GCCM is used to identify orthorhombic representations of a monoclinic crystal and some computational advantages of using an orthorhombic representation in molecular dynamics simulations are demonstrated. The GCCM is used to prepare simulation cells containing grain boundaries in monoclinic β-HMX crystals. The ranking order of their stabilities is predicted to correlate with the relative prominence of constituent crystal faces observed in an experimental study of β-HMX crystal habits and morphologies. The GCCM is applied to the construction of starting configurations for nanowires and icosahedral nanoparticles exhibiting five-fold twinned structures for subsequent molecular dynamics simulations. Additional example GCCM constructions are shown that could help address relevant materials science problems in areas including explosives, organic semiconductors, and pharmaceuticals.

Acknowledgments

The authors thank Markus Fröhlich for pre-release access to modifications for the HMX force field. The U.S. Air Force Office of Scientific Research supported this research under Grant No. FA9550-14-1-0360.

Please cite this article in press as: M.P. Kroonblawd, et al., A generalized crystal-cutting method for modeling arbitrarily oriented crystals in 3D periodic simulation cells with applications to crystal–crystal interfaces, Computer Physics Communications (2016), http://dx.doi.org/10.1016/j.cpc.2016.07.007

Appendix A. Supplementary Material

Supplementary Material related to this article can be found online at http://dx.doi.org/10.1016/j.cpc.2016.07.007.

References

[1] K.J. Ramos, D.E. Hooks, T.D. Sewell, M.J. Cawkwell, J. Appl. Phys. 108 (2010) 066105.
[2] L. Munday, Computational study of the structure and mechanical properties of the molecular crystal rdx (Ph.D. thesis), University of Maryland, College Park, 2011.
[3] D. Wang, L. Tang, M. Long, Z. Shuai, J. Phys. Chem. C 115 (2011) 5940–5946.
[4] L. He, T.D. Sewell, D.L. Thompson, J. Chem. Phys. 136 (2012) 034501.
[5] Q. An, Y. Liu, S.V. Zybin, H. Kim, W.A. Goddard III, J. Phys. Chem. C 116 (2012) 10198–10206.
[6] T. Zhou, S.V. Zybin, Y. Liu, F. Huang, W.A. Goddard III, J. Appl. Phys. 111 (2012) 124904.
[7] M.P. Kroonblawd, T.D. Sewell, J. Chem. Phys. 139 (2013) 074503.
[8] D. Guo, Q. An, W.A. Goddard III, S.V. Zybin, F. Huang, J. Phys. Chem. C 118 (2014) 30202–30208.
[9] N. Mathew, T.D. Sewell, Phil. Mag. 95 (2015) 424–440.
[10] N. Mathew, T.D. Sewell, D.L. Thompson, J. Chem. Phys. 143 (2015) 094706.
[11] J.E. Northrup, M.L. Tiago, S.G. Louie, Phys. Rev. B 66 (2002) 121404.
[12] R.H. Gee, A. Maiti, S. Bastea, L.E. Fried, Macromolecules 40 (2007) 3422–3428.
[13] F.R. Massaro, M. Moret, M. Bruno, D. Aquilano, Cryst. Growth Des. 12 (2012) 982–989.
[14] C.L. Cleveland, W.D. Luedtke, U. Landman, Phys. Rev. Lett. 81 (1998) 2036–2039.
[15] H.S. Nam, N.M. Hwang, B.D. Yu, J.K. Yoon, Phys. Rev. Lett. 89 (2002) 275502.
[16] A. Cao, Y. Wei, Phys. Rev. B 74 (2006) 214108.
[17] J.H. Yoo, S.I. Oh, M.S. Jeong, J. Appl. Phys. 107 (2010) 094316.
[18] S. Jiang, Y. Shen, Y. Zheng, Z. Chen, Appl. Phys. Lett. 103 (2013) 041909.
[19] S. Jiang, Z. Chen, H. Zhang, Y. Zheng, H. Li, Int. J. Mult. Comp. Eng. 11 (2013) 1–16.
[20] P. Keblinski, S.R. Phillpot, D. Wolf, H. Gleiter, Phys. Rev. Lett. 77 (1996) 2965–2968.
[21] O.A. Shenderova, D.W. Brenner, L.H. Yang, Phys. Rev. B 60 (1999) 7043–7052.
[22] S. Kodiyalam, R.K. Kalia, H. Kikuchi, A. Nakano, F. Shimojo, P. Vashishta, Phys. Rev. Lett. 86 (2000) 55–58.
[23] J. Schiøtz, K.W. Jacobsen, Science 301 (2003) 1357–1359.
[24] P.K. Schelling, S.R. Phillpot, P. Keblinski, J. Appl. Phys. 95 (2004) 6082.
[25] D. Wolf, V. Yamakov, S.R. Phillpot, A. Mukherjee, H. Gleiter, Acta Mater. 53 (2005) 1–40.
[26] S. Verlaak, P. Heremans, Phys. Rev. B 75 (2007) 115127.
[27] O.V. Yazyev, S.G. Louie, Nature Mater. 9 (2010) 806–809.
[28] Y. Long, Y.G. Liu, F.D. Nie, J. Chen, Modell. Simul. Mater. Sci. Eng. 20 (2012) 065010.
[29] K.R. Hahn, M. Puligheddu, L. Colombo, Phys. Rev. B 91 (2015) 195313.
[30] K.-H. Lin, A. Strachan, J. Chem. Phys. 143 (2015) 034703.
[31] M. Haisa, S. Kashino, H. Maeda, Acta Crystallogr. B 30 (1974) 2510–2512.
[32] M. Haisa, S. Kashino, R. Kawai, H. Maeda, Acta Crystallogr. B 32 (1976) 1283–1285.
[33] H.H. Cady, A.C. Larson, Acta Crystallogr. 18 (1965) 485–496.
[34] C.S. Choi, H.P. Boutin, Acta Crystallogr. B 26 (1970) 1235–1240.
[35] O. Bolton, A.J. Matzger, Angew. Chem. Int. Ed. 50 (2011) 8960–8963.
[36] O. Bolton, L.R. Simke, P.F. Pagoria, A.J. Matzger, Cryst. Growth Des. 12 (2012) 4311–4314.
[37] C.C. Mattheus, A.B. Dros, J. Baas, A. Meetsma, J.L. de Boer, T.T.M. Palstra, Acta. Cryst. C 57 (2001) 939–941.
[38] S. Schiefer, M. Huth, A. Dobrinevski, B. Nickel, J. Am. Chem. Soc. 129 (2007) 10316–10317.
[39] C. Ophus, A. Shekhawat, H. Rasool, A. Zettl, Phys. Rev. B 92 (2015) 205402.
[40] F. Müller-Plathe, J. Chem. Phys. 106 (1997) 6082–6085.
[41] V. Vítek, Phil. Mag. 18 (1968) 773–786.
[42] A.P. Sutton, R.W. Balluffi, Interfaces in Crystalline Materials, Clarendon Press, Oxford, United Kingdom, 1995.
[43] Y.T. Zhu, X.Z. Liao, R.Z. Valiev, Appl. Phys. Lett. 86 (2005) 103112.
[44] I.T. Todorov, W. Smith, K. Trachenko, M.T. Dove, J. Mater. Chem. 16 (2006) 1911–1918.
[45] B. Hess, C. Kutzner, D. van der Spoel, E. Lindahl, J. Chem. Theory Comput. 4 (2008) 435–447.
[46] S. Plimpton, J. Comput. Phys. 117 (1995) 1–19.
[47] J.C. Phillips, R. Braun, W. Wang, J. Gumbart, E. Tajkhorshid, E. Villa, C. Chipot, R.D. Skeel, L. Kalé, K. Schulten, J. Comput. Chem. 26 (2005) 1781–1802.
[48] G.D. Smith, R.K. Bharadwaj, J. Phys. Chem. B 103 (1999) 3570–3575.
[49] R.W. Hockney, J.W. Eastwood, Computer Simulation Using Particles, CRC Press, Boca Raton, FL, 1988.
[50] W.M. Brown, P. Wang, S.J. Plimpton, A.N. Tharrington, Comput. Phys. Commun. 182 (2011) 898–911.
[51] W.M. Brown, A. Kohlmeyer, S.J. Plimpton, A.N. Tharrington, Comput. Phys. Commun. 183 (2012) 449–459.
[52] W.M. Brown, Y. Masako, Comput. Phys. Commun. 184 (2013) 2785–2793.
[53] H.G. Gallagher, J.N. Sherwood, R.M. Vrcelj, Chem. Cent. J. 8 (2014) 75.
[54] E. Bitzek, P. Koskinen, F. Gähler, M. Moseler, P. Gumbsch, Phys. Rev. Lett. 97 (2006) 1–4.
[55] W. Humphrey, A. Dalke, K. Schulten, J. Mol. Graphics 14 (1996) 33–38.
[56] A. Stukowski, Model. Simul. Mater. Sci. Eng. 18 (2009) 015012.
[57] H. Hofmeister, Cryst. Res. Technol. 33 (1998) 3–25.
[58] B. Wu, A. Heidelberg, J.J. Boland, X.M. Sun, Y.D. Li, Nano Lett. 6 (2006) 468–472.
[59] X.Z. Liao, Y.H. Zhao, S.G. Srinivasan, Y.T. Zhu, R.Z. Valiev, D.V. Gunderov, Appl. Phys. Lett. 84 (2004) 592–594.
[60] B. Wu, A. Heidelberg, J.J. Boland, Nature Mater. 4 (2005) 525–529.
[61] L. Zhu, X. Shen, Z. Zeng, H. Wang, H. Zhang, H. Chen, ACS Nano 6 (2012) 6033–6039.
[62] J.A. Ascencio, C. Gutiérrez-Wing, M.E. Espinosa, M. Marin, S. Tehuacanero, C. Zorrilla, M. José-Yacamán, Surf. Sci. 396 (1998) 349–368.
[63] T. Shen, Y. Wu, X. Lu, J. Mol. Model. 19 (2013) 751–755.
[64] S. Nosé, J. Chem. Phys. 81 (1984) 511–519.
[65] W.G. Hoover, Phys. Rev. A 31 (1985) 1695–1697.
[66] M.S. Daw, M.I. Baskes, Phys. Rev. B 29 (1984) 6443–6453.
[67] S.M. Foiles, M.I. Baskes, M.S. Daw, Phys. Rev. B 33 (1986) 7983–7991.
[68] J.L. Brédas, J.P. Calbert, D.A. da Silva Filho, J. Cornil, Proc. Natl. Acad. Sci. 99 (2002) 5804–5809.
[69] J.H. Kang, D. da Silva Filho, J.-L. Brédas, X.-Y. Zhu, Appl. Phys. Lett. 86 (2005) 152115.
[70] V. Kalihari, E.B. Tadmor, G. Haugstad, C.D. Frisbie, Adv. Mater. 20 (2008) 4033–4039.
[71] S. Seo, P.G. Evans, J. Appl. Phys. 106 (2009) 103521.
[72] P. Di Martino, A.-M. Guyot-Hermann, P. Conflant, M. Drache, J.-C. Guyot, Int. J. Pharm. 128 (1996) 1–8.
[73] J.-M. Fachaux, A.-M. Guyot-Hermann, J.-C. Guyot, P. Conflant, M. Drache, S. Veesler, R. Boistelle, Powder Technol. 82 (1995) 129–133.
[74] J.D. Yeager, K.J. Ramos, N.H. Mack, H.-L. Wang, D.E. Hooks, Cryst. Growth Des. 12 (2012) 5513–5520.

Please cite this article in press as: M.P. Kroonblawd, et al., A generalized crystal-cutting method for modeling arbitrarily oriented crystals in 3D periodic simulation cells with applications to crystal–crystal interfaces, Computer Physics Communications (2016), http://dx.doi.org/10.1016/j.cpc.2016.07.007